Journal of Structural Dynamics

Experimental Development of Nonlinear Transfer Function Measurements

Caleb Bengs [*1], Daniel Roettgen [†2], and Benjamin Moldenhauer [‡2]

[1] *Texas A&M University College of Engineering, Department of Aerospace Engineering, 3127 TAMU, College Station, TX 77843-3127*
[2] *Sandia National Laboratories, P.O. Box 5800 – MS0557, Albuquerque, NM 87185*

Abstract

Modal analysis is the primary means of analyzing structural responses to external forcing, informing decision-making or further physical testing of the structure. Nevertheless, most commercially available solutions assume the test article behaves linearly with excitation amplitude. If significant amounts of nonlinear stiffness or damping are present in the structure, large errors in linear analysis may result which could lead to improper decisions that may be costly. Therefore, it is useful to develop experimental techniques or computational models which account for nonlinearity during modal analysis. This paper describes a method of generating frequency response functions at various excitation energy levels to generate a three-dimensional transfer function surface. The resulting transfer function surface is agnostic of drive-point location, allowing excitations at different drive points to be compared directly. This result holds only if the drive point is sufficiently far from node points. The Brake-Reuß beam is used as the experimental exemplar at various levels of impact testing. Best practices learned during experimentation are included.

Keywords: Nonlinear Dynamics; Frequency Response Functions; Nonlinear Modal Modeling

Received on April 15, 2025, Accepted on February 19, 2026, Published on March 10, 2026

1 Introduction

1.1 Work Overview

The frequency response function (FRF) is often used to study the dynamic response of linear systems due to the ease with which it can be obtained and the breadth of information it provides. However, the majority of real systems exhibit some degree of nonlinear behavior, and it is becoming increasingly important to characterize their nonlinear performance. A variety of analytical and experimental techniques have been developed for this purpose [1, 2, 3, 4, 5, 6, 7, 8, 9, 10, 11, 12, 13, 14, 15, 16, 17, 18, 19, 20, 21, 22, 23, 24]. Many of these models, such as Feldman's FREEVIB model [14], assume polynomial models of stiffness and damping [17]. Other methods involve parametric approaches, such as the use of modal Iwan elements in parallel with typical spring-mass-damper elements [15, 16, 17, 18, 19, 20, 21, 22, 23, 24].

This paper introduces a new method of characterizing nonlinear behavior in structures, the outcome of which is comparable to the existing model-based approaches. Instead of creating a new model, the approach develops a three-dimensional FRF surface that relates frequency, response amplitude, and excitation energy. The surface is termed a performance surface FRF (PSFRF); it provides a visual method useful for quickly characterizing the

[*] calebbengs@tamu.edu
[†] drroett@sandia.gov
[‡] bmolden@sandia.gov

nonlinear behavior of a structure while also retaining the computational flexibility required for more robust numerical calculations. The creation of a PSFRF is demonstrated on a Brake-Reuß beam [25, 26, 27]. The Brake-Reuß beam is composed of two halves connected with three bolts via a lap joint. In this work, the bolts are tightened to 100 lbf-in using a calibrated torque wrench. The Brake-Reuß beam is used due to the breadth of knowledge available concerning its nonlinearities, making it a perfect candidate for validating a new nonlinear method. This study is concerned solely with bending modes obtained at high preload levels, so the Brake-Reuß beam behavior is expected to be weakly nonlinear (the change in stiffness is small and modal coupling insignificant with increasing excitation amplitude) [27]. Despite this, the method still works for strong or large changes in damping, as shown in the case of the Brake-Reuß beam. Furthermore, the beam exhibits softening behavior in which damping increases and frequency decreases with increasing excitation amplitude. Hence, any valid nonlinear method should accurately capture the weakly nonlinear softening behavior of the beam.

To create a PSFRF, the mode shapes are first extracted through a series of low-level impact tests. This data is used to create a mode shape matrix associated with the Brake-Reuß beam. Next, a series of impact tests spanning a dynamic range of 0-250 lbf is conducted for two drive points. This data is processed in physical space, resulting in the production of PSFRFs which are used to verify the accurate capture of nonlinear behavior. Once the behavior of the PSFRFs are verified, the data is converted to the modal space using an appropriate modal model. This is done to render the resulting modal PSFRFs (MPSFRFs) agnostic of excitation location. These MPSFRFs, created for each mode and drive point under consideration, are then compared to determine the validity of this agnosticism. Finally, additional data-processing techniques are used to streamline the appearance of the MPSFRFs; the accuracy of these surfaces is assessed.

1.2 Literature Review

The method of FRFs is a highly useful tool for categorizing the behavior of a structure's dynamic response to a variety of input excitations. In many cases, it allows the researcher to quickly and simply estimate a system's characteristics and use them to update the system model. Nevertheless, most systems are nonlinear. As a result, many methods have been invented which attempt to account for these nonlinearities. References [28] and [29] constitute a thorough review documenting system identification methods invented to deal with nonlinear structures. Due to the breadth of studies conducted in this area and the comprehensive reviews on such studies that already exist (such as [28, 29]), an in-depth explanation of all nonlinear methods heretofore developed will not be given. Instead, an overview of how the new method differs from similar methods in the field is presented. Because this field is dynamic and there exist a multitude of crossovers between different methods, the exclusion of any relevant methods is unintentional.

The MPSFRFs that result from the new method are three-dimensional extensions of FRFs. Therefore, the new method is immediately differentiated from harmonic force balance methods (or describing function methods), restoring force methods, the FREEVIB method, force appropriation, and finite element methods [14, 13, 30, 31, 32, 33, 34, 35]. Nevertheless, there are still many techniques with similar intent or output which must be differentiated from the new method. These include nonlinear autoregressive moving average with exogenous inputs (NARMAX) modeling, nonlinear FRFs (NOFRFs), nonlinear normal modes, waterfall plots, spectrograms, and frequency response curves. The latter are used more recently in new techniques involving control-based continuation (CBC) and response-controlled stepped-sine testing (RCT).

First, MPSFRFs are generated by evaluating linear FRFs from experimental data and creating an aggregate 3D surface in modal space which is a function of both frequency and energy level (similar to a waterfall plot). The physical linear FRFs used to create the MPSFRFs are not obtained from a model or any form of series expansion, though a pseudo-inverse is used to transform the physical FRFs into the modal space. Nevertheless, the process of experimentally obtaining linear FRFs immediately distinguishes the MPSFRF method from the NARMAX method and its derivatives because the NARMAX method fundamentally represents the conversion of a differential equation into a discrete-time equation which can be used to evaluate system behavior [36, 37]. Furthermore, the MPSFRF method is distinguished from generalized frequency response functions (GFRFs, also known as higher-order frequency response functions) and their derivatives (such as NOFRFs) because it does not involve the use of convergent Volterra or Weiner series [38, 39, 40, 41, 42, 43].

Nonlinear normal modes are extensions of the traditional linear normal modes that allow the behavior of nonlinear objects to be composed as the superposition of these nonlinear modes [43, 44, 45]. However, nonlinear normal modes may exchange energy as a result of internal resonances, making it a helpful tool for studying nonlinear effects such as energy localization and transfer [46, 47, 48, 49]. Two popular methods of analyzing nonlinear normal modes involve the use of empirical mode decomposition (EMD) and proper orthogonal decomposition (POD) which assume a time series can be decomposed into fast-time and slow-time harmonic components representing monochromatic

oscillations and amplitude variation, respectively [50, 51, 52]. Both EMD and POD can be used to identify the behavior of strongly nonlinear attachments to linear systems, even identifying internal resonances of modes that are not rationally related [51, 52]. Unlike EMD and POD, MPSFRFs have only been verified for weakly nonlinear systems. Nevertheless, MPSFRFs are valid for intrinsically nonlinear systems while EMD and POD are best suited for studying local nonlinearities.

This work highlights a proposed technique to extract nonlinear transfer functions using both input and output measurements to characterize a nonlinear mechanical system. This is completed using a Fourier analysis approach but considers both input force and excitation amplitude, where other methods (like ZEFFT [53] and STFT [54]) operate on output only information and may require less testing. With MPSFRFs an input force can be used to estimate an output response, but requires additional testing and bookkeeping to create a usable transfer function model.

Waterfall plots are three-dimensional plots of a structure's frequency response created by obtaining linear FRFs at a multitude of different excitations (or some other parameter) and stitching those responses together in order of ascending excitation (parameter) level. The resulting plot gives a picture of the response of the structure as a function of frequency and the excitation (parameter) value. Di Maio creates a plot termed the nonlinear frequency response surface which is essentially a waterfall plot of linear FRFs plotted against a third axis of displacement [55]. The nonlinearity of the structure is exhibited by the associated 2D color-spectrum plot of frequency versus displacement (which resembles a spectrogram). The results obtained by Di Maio resemble the physical space PSFRFs obtained in the current study, though Di Maio uses displacement as the third axis and the authors use excitation energy. While waterfall plots (such as the nonlinear frequency response surface created by Di Maio and the PSFRFs developed in the current study) are useful for obtaining information about the nonlinear behavior of a particular structure, these plots are highly dependent upon the excitation location; the FRFs will shift and deform if the excitation location is varied while the excitation amplitude remains constant. This is due to the fact that waterfall plots are created in the physical space. MPSFRFs, on the other hand, are created in the modal space, rendering them drive-point agnostic (they exhibit little change if excitation location is varied). This shift to the modal space marks the most fundamental difference between the current method and that developed by Di Maio. Finally, the MPSFRFs can be rotated to obtain a 2D color-spectrum view of frequency versus excitation which serves as a spectrogram of the nonlinear information.

Frequency response curves represent the response of a structure to the changing frequency of an imposed periodic excitation. Therefore, these plots differ immediately from the MPSFRFs since only modal hammer excitation is used in the current study. Furthermore, though Di Maio uses a sinusoidal excitation to create his nonlinear frequency response curves, the linear FRFs are created by varying force level, not excitation frequency [55]. Although future work regarding the creation of MPSFRFs with shaker data may be able to utilize frequency response curves, the current study uses FRFs created from single modal hammer impacts only.

2 Background

2.1 Modal Filter

The conversion of data from physical space to modal space is performed with a modal filter of the type:

$$\mathbf{\Phi}^{+}\ddot{\mathbf{x}} = \ddot{\mathbf{q}} \tag{1}$$

where the matrix $\ddot{\mathbf{x}}$ contains physical response data, the matrix $\ddot{\mathbf{q}}$ contains the modal response data, and the matrix $\mathbf{\Phi}^{+}$ is the pseudo-inverse of the extracted mode shape matrix. In the context of experimental testing of a real object, the matrix $\mathbf{\Phi}^{+}$ has the dimensions $M \times S$ where M is the number of modes considered and S is the number of sensors in use. Because $\ddot{\mathbf{x}}$ contains physical response data for the sensors at N distinct points in time, the matrix $\ddot{\mathbf{q}}$ will have dimensions $M \times N$. By using this filter, the authors assume the mode shapes under consideration are well-separated. Ref. [56] contains a more detailed explanation of the modal filter.

2.2 RMS Percent Error

Two different error metrics are used to compare the similarity of different PSFRFs. The first metric is adapted from the root-mean-square (RMS) percent error metric presented in Marinone and Moya [57]. The RMS percent error technique is a way of assessing the difference in total energy content captured by two FRFs. First, a discrete set of frequency values are considered, and the square of the FRF amplitude is determined for each value in this frequency

set. Then, the square root of the sum of the squares gives the RMS value for the FRF. Finally, the percent difference of the RMS values for two FRFs is given by Eq. 2.

$$\%\ Difference\ RMS = \frac{|RMS_1 - RMS_2|}{\frac{1}{2}(RMS_1 + RMS_2)} \cdot 100 \tag{2}$$

The result of Eq. 2 represents the percent difference in energy content captured by two FRFs.

2.3 Cross Signature Assurance Criterion

The second metric used to compare the similarity of different PSFRFs is adapted from the cross signature assurance criterion (CSAC) also presented in Marinone and Moya [57]. Unlike the RMS percent error metric, the CSAC is used to determine the similarity of shape between two FRFs. The CSAC metric is given by Eq. 3.

$$CSAC = \frac{|H_1^H(\omega_k)H_2(\omega_k)|^2}{(H_1^H(\omega_k)H_1(\omega_k)) \cdot (H_2^H(\omega_k)H_2(\omega_k))} \tag{3}$$

In Eq. 3, $H_1(\omega_k)$ represents a vector of values of the first FRF at each of the frequencies ω_k under consideration, and $H_2(\omega_k)$ represents a vector of values of the second FRF at the same frequency values. A superscript H indicates the vector contains the transposed complex conjugates of the values in the original vector. The CSAC takes on a range of values from 0 to 1, inclusive; a CSAC of 1 indicates total shape similarity while lower CSAC values indicate more sharply diverging shapes.

3 Methodology

3.1 Test Structure

The Brake-Reuß beam is used as the test structure, and its geometry and dimensions are shown in Fig. 1. Each bolt is torqued to 100 lbf-in. The global coordinate system of the beam is established with the *x*-axis lying along the length of the beam, the *z*-axis oriented perpendicular to the *x*-axis and parallel with the bolts with the positive direction pointing towards the bolt heads, and the *y*-axis completing the right-handed triad. Eight tri-axial accelerometers are attached to the positive *z*-face of the beam, arranged in a line along the *x*-direction. Sensors 101-106 are oriented with their local coordinate systems aligned to the global coordinate system. The local coordinate systems of sensors 107 and 108 are oriented with the *x*-axes in the direction of the negative global *x*-axis, the *y*-axes in the direction of the negative global *y*-axis, and the *z*-axes aligned with the global *z*-axis. The accelerometers are each model 356A03 units produced by PCB Piezotronics with nominal sensitivities of 10 mV/g. A model 086C03 modal hammer produced by PCB Piezotronics with a nominal sensitivity of 10 mV/lbf is used to excite the test structure. The accelerometer and force data are recorded with the Rattlesnake Vibration Controller software created by Dan Rohe at Sandia National Laboratories [58].

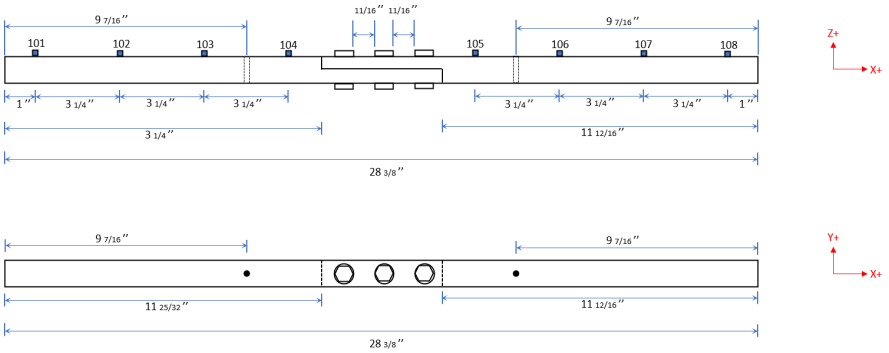

Fig. 1: Brake-Reuß Beam Geometry with Sensor Placement

Four drive points are used for test object excitation in order to ensure test repeatability. Each drive point is located on the negative *z*-face of the test object at positions reflected across the *xy*-plane from the sensor positions. So, drive point 1 is associated with sensor 101, drive point 2 with sensor 102, drive point 3 with sensor 103, and drive point 5 with sensor 105 (drive point 4 is omitted so the drive point numbers will match the sensor positions). The line-of-action of drive point 1 extends from its origin on the negative *z*-face through the center of sensor 101.

3.2 Mode Shape Determination

The creation of PSFRFs requires knowledge of the linear mode shapes of the test structure. The mode shape information is extracted by capturing ten low-level hammer hits (between 0-10 lbf) at drive point 1 with the Rattlesnake Vibration Controller software. This data is then loaded into the PolyPy GUI application provided by the SDynPy package created by Dan Rohe [58]. In the PolyPy GUI, the natural frequency and damping ratio of each mode are determined and saved to a data file. In this paper, the cutoff frequency is 1400 Hz. At this frequency, only the first three modes associated with the *z*-axis are captured. Higher cutoff frequencies are not considered because this paper is concerned with the verification of MPSFRFs as a viable method of characterizing nonlinearities, not with exhaustively characterizing the nonlinearities of the Brake-Reuß beam.

3.3 Data Collection

The data is collected by striking the test object with a modal hammer. All testing and results, unless otherwise indicated, are collected on the same day to reduce the effects of day-to-day variances and resettling differences in the data. First, 250 hammer hits are recorded for drive point 1. The force level of all hammer hits collected are contained in the range of 0-250 lbf. Next, 250 hammer hits are recorded separately for drive points 2 and 3, using the same range of force levels previously established. Finally, ten hammer hits at drive point 5 are collected at random levels between 0 lbf and 250 lbf.

Before proceeding, it is worth noting that 250 hammer hits is extensive. This is done to emphasize the contributions of the nonlinear response. Industrial practitioners should consider using FRF smoothing techniques such as Ref. [59] or an automated modal hammer to scale input level and reduce excessive data requirements.

3.4 Experimental Considerations

To ensure the PSFRFs and MPSFRFs accurately capture the weakly nonlinear softening behavior of the Brake-Reuß beam, a broad excitation range is considered. The initial method of excitation proceeded by performing ten impacts within 10-lbf intervals and saving each set of data in individual files (e.g. ten impacts in the range of 0-10 lbf, then 10-20 lbf, etc.). Due to the small force ranges, it took a significant amount of time to obtain ten strikes in each range, and settling behavior was clearly observed in the experiment. To overcome this difficulty, the authors excite each drive point by incrementally varying strikes from lower to higher force levels without targeting a particular force range. Once the maximum force level is approached, the tester again starts from a low force level and progressively increments the force. This “full sweep" of the energy range is repeated approximately three times in the course of 250 strikes (per drive point). The data is then sorted based on energy content. As a result, testing is conducted in a fraction of the original time, eliminating the settling differences. Though excitation in a more “random" manner makes it more difficult to obtain energy "bins" of equal size, the large quantity of data ensures the whole excitation range is explored with some degree of uniformity.

An additional experimental consideration is wear in the bolted interfaces. As indicated in the Data Collection section, this study involved a very large number of hammer impacts. Because high amplitudes or prolonged testing can cause damage over time, the test object was monitored by testing the specimen at low load levels to excite linear dynamics at the beginning and end of each test series. This ensured the linear parameters of the system were not shifting due to wear over the course of the study. To potentially reduce data and testing requirements, practicioners are once again referred to FRF smoothing techniques such as Ref. [59].

3.5 Proof of Concept - The Creation of Physical Space PSFRFs

After data collection, PSFRFs are first created in the physical space as a proof of concept. The creation of a PSFRF consists of four main stages: importing data into a computer, sorting the data according to maximum hammer excitation level, creating individual FRFs from each set of hammer impact data, and stitching the individual FRFs

together to create a three-dimensional performance surface envelope (the PSFRF). The steps in this process are represented briefly in the flowchart in Fig. 2, and the resulting PSFRF is shown in Fig. 3. The steps to create a PSFRF will now be discussed in more detail; the process is the same regardless of the drive point considered.

The first step in the creation of the PSFRF is to load the data to an appropriate computer software. Although PSFRFs can be created with the help of multiple programming languages, Python is a natural choice because it is an open-source software, making it a simple and cost-effective strategy. Furthermore, the SDynPy Python package contains many useful tools for reading and processing data collected by the Rattlesnake Vibration Controller software.

After loading the experimental data, it is sorted with respect to the maximum force value recorded during each impact measurement. Despite the high sampling-rate used to capture the hammer impact and response data, it is still possible that the true maximum impact level is lost due to the digital sampling of the hammer voltage during collection. Since the data is sorted with respect to maximum hammer impact, it is desirable to estimate the true maximum impact level for each set of data. This is accomplished by determining the Fast Fourier Transform (FFT) of the hammer data for each impact and up-sampling them by a specified number. For this experiment, all FFTs of the impact data are up-sampled to increase the sample rate of the hammer data ten-fold. Next, the up-sampled FFTs are subjected to an inverse FFT to obtain the time-history data with an increased resolution. These hammer impact time-histories are then used to create a list of corresponding maximum impact forces. This list is used to reorder the datasets in ascending order of maximum impact level. This completes the sorting process in the physical domain. Note, the FFT can be seen as an averaging or smoothing of the nonlinearity across the experimental time series. This can deteriorate the visual appearance of the strength of the nonlinearity but preserves the information about the nonlinearity and is reversible using an inverse Fast Fourier Transform.

Once the data is sorted, the z-directional data is parsed from the response data set. Next, the reference data (hammer impact time-histories) and response data are used to create FRFs for each dataset. To increase the frequency resolution of the PSFRFs, the time-data can be zero-padded prior to computing the FFTs and creating the subsequent FRFs. Finally, the individual FRFs are plotted versus their corresponding values of maximum hammer impact. This results in a three-dimensional PSFRF as shown in Fig. 3a. To show that a PSFRF successfully captures nonlinear behavior, small intervals around the natural frequencies are considered separately. A zoomed-in view of the second mode of the experiment is exhibited in Fig. 3b. As the excitation amplitude increases, the maximum response amplitude and frequency at which this maximum is obtained decreases. Therefore, the PSFRFs successfully capture the predicted nonlinear softening behavior of the Brake-Reuß beam. Please note the amplitude data of both figures is reported in log base-10. All future figures with log axes are reported in log base-10 as well.

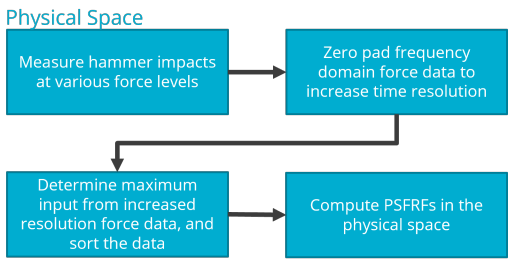

Fig. 2: Flowchart for PSFRF Creation

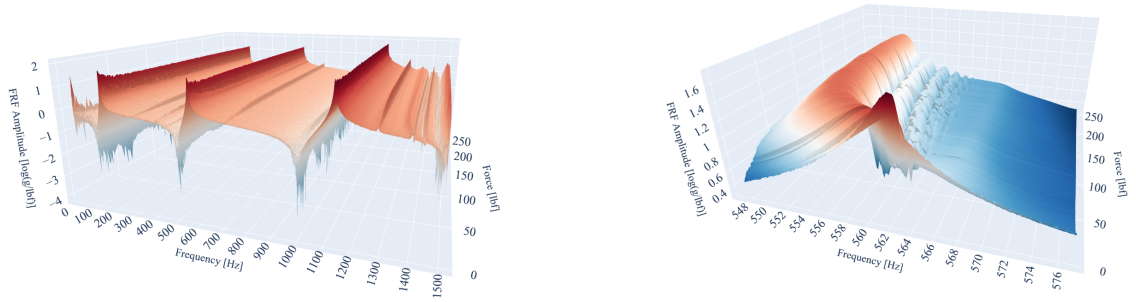

(a) Full PSFRF

(b) Zoomed-In PSFRF of Mode 2

Fig. 3: PSFRF from Drive Point 1 Data

3.6 Modal Performance Surface FRFs (MPSFRFs)

Although physical space PSFRFs accurately capture the linear and nonlinear behavior of the test object, they are narrowly useful at making behavioral predictions. The behavior of a PSFRF in the modal space (a MPSFRF) should

theoretically be drive point agnostic, increasing the scope of predictability. Hence, a separate process for creating MPSFRFs is detailed. The steps in this process are briefly summarized in the flowchart in Fig. 4, and the resulting MPSFRFs are shown in Fig. 5.

Like the creation of a PSFRF, the creation of a MPSFRF begins by sorting the data. However, the data-sorting process for MPSFRF-construction is different. When considering a PSFRF, the data is sorted according to maximum impact force. Although sufficient for the purposes of proof-of-concept, the maximum impact force does not always accurately reflect the total energy imparted to the test object. A better metric of the energy transfer is the area under the auto power spectral density (APSD) of the reference data. Hence, in the creation of a MPSFRF, the data is sorted according to the area under the APSD plot.

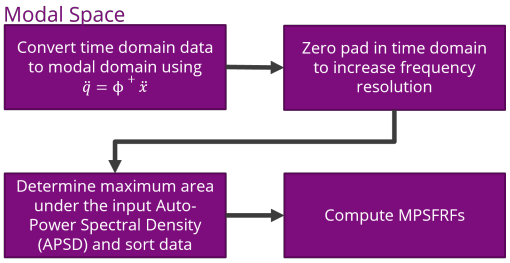

Fig. 4: Flowchart for MPSFRF Creation

After reading the data into Python, the reference and response data are converted to the modal space via Eq. 1. Then, the reference and response data associated with each mode shape are separated. This separation of modes means a single PSFRF is represented by a number of MPSFRFs equal to the number of distinct modes being examined. In the case of this study, the number is three. The remaining steps are completed for each mode under consideration. Using the modal data, a FRF is created for each dataset. The natural frequencies of the modal FRFs are determined, and small intervals around the natural frequencies are selected. For this experiment, a frequency interval of ± 15 Hz was used for each dataset. Next, the APSD of the reference data in the frequency intervals are approximated using Simpson's rule. This process allows only the energy content in the immediate vicinity of the natural frequency to be included, reducing potential contributions from other resonance peaks. Then, the datasets are sorted in ascending order according to the associated APSD area values. Finally, the sorted modal FRFs are stitched together to create a MPSFRF.

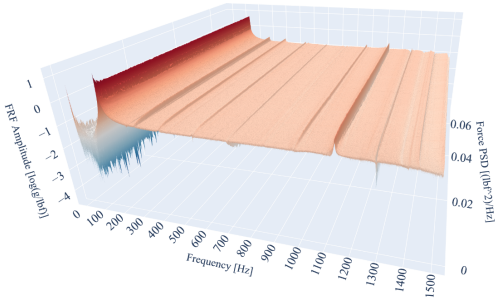

(a) Mode 1

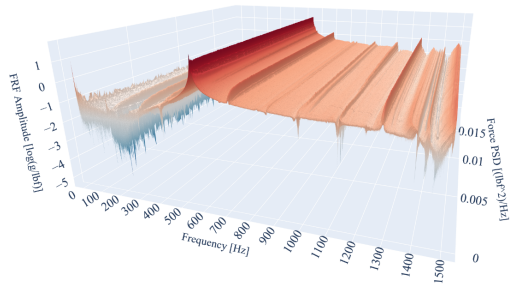

(b) Mode 2

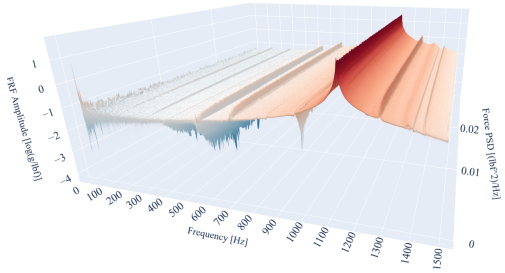

(c) Mode 3

Fig. 5: MPSFRFs from Drive Point 1 Data

Before proceeding to the validation, it is important to emphasize that the spatial filter implemented in Eq. 1

(the modal filter) is used to transform the collected data from the physical space to the modal space as one of the steps in the creation of MPSFRFs. Due to the nature of the modal filter, the presence of significant modal coupling could decrease the quality of this filtering technique and consequently the MPSFRFs. In the case of this study, the mode shapes considered remained constant and use of the modal filter is valid. Before using this method to create MPSFRFs, practitioners should confirm that pronounced modal coupling is not present in the test data.

4 Validation

4.1 Verification that MPSFRFs are Drive Point Agnostic

In order to verify that MPSFRFs are drive point agnostic, two MPSFRFs are created for each of the modes under consideration, one from drive point 1 data and the other from drive point 2 data. To compare MPSFRFs, the same set of points must be considered for each performance surface. Because this is impossible to do with manual hammer impact testing, computational methods must be employed to compare the data. This is accomplished with the *griddata* method contained in the SciPy Python library. First, MPSFRFs representing the same mode are selected. Then, the excitation amplitude of the two surfaces are compared; the maximum excitation amplitude is different for distinct surfaces due to scaling of the reference data when transforming surfaces into the modal space. The surface with the smallest maximum value of excitation amplitude is selected, and a mesh of equally spaced points is placed over the plane of frequency versus excitation amplitude. The same mesh is also applied to the other MPSFRF. Next, the amplitudes of each point in the meshes were determined. In the case that a point on a mesh does not coincide with a known datapoint, linear interpolation between datapoints is used to approximate the values at the mesh coordinates. After grids of amplitude values are obtained for each of the MPSFRFs, they are directly compared.

As mentioned in Section 2, the RMS percent error metric and CSAC metric are used to compare different MPSFRFs. Having a low RMS percent error metric indicates that FRFs are similar in energy content, and a high CSAC metric indicates that FRFs are similar in shape. Nevertheless, because the RMS percent error and CSAC metrics are used to compare 2D FRFs, additional processes are required to adapt these metrics for use with 3D MPSFRFs. For the RMS percent error metric, the RMS of each FRF composing an MPSFRF is determined. Then, the mean value of the RMS is calculated. Once this is completed for both surfaces, the mean RMS values are used in Eq. 2. Using data from the amplitude grids, this process is repeated by frequency line as well as by individual FRF. This enables the assessment of the total energy content captured by different MPSFRFs using two different bases: excitation energy (or for each individual FRF), and frequency level. For the CSAC metric, the CSAC value is determined for each individual FRF composing a MPSFRF. Then, the average CSAC value is determined and used as a representative value for the MPSFRF. Fig. 6 and Fig. 7 show plots of the RMS and CSAC values, respectively, determined for drive points 1 and 2 data. The mean RMS and CSAC values are displayed on their respective plots.

As shown in Table 1, the RMS percent differences by both excitation energy and frequency line are less than one percent for mode 1 and mode 3. In other words, the total energy levels encapsulated by the MPSFRFs from drive points 1 and 2 for modes 1 and 3 are almost identical. Furthermore, the mean CSAC values for modes 1 and 3 are close to 1, signifying the shapes of the MPSFRFs are similar. This strongly supports the claim that MPSFRFs are drive point agnostic. Fig. 6 reveals the largest discrepancies in shape to be in the local area of the linear natural frequency. This may be due to small settling differences in experimental assembly, but further testing is required to evaluate this conclusion.

Nevertheless, at first glance, the metrics associated with mode 2 seem to imply large differences in the MPSFRFs. The RMS percent differences for mode 2 (by energy level and frequency) are both above 7% (as seen in Fig. 6c and Fig. 6d), and the CSAC is below 0.9 (as seen in Fig. 7b). Further exploration revealed the physical location of drive point 2 is located close to one of the nodes associated with mode 2. As a result, the conversion to modal space causes the mode 2 excitation from drive point 2 to scale onto the linear portion of the corresponding figure of drive point 1. This causes the comparison metrics to deteriorate rapidly and accounts for the inconsistency.

4.2 Averaged MPSFRFs

The previous section demonstrates that MPSFRFs created using data from different drive points are agnostic of excitation location. As a result, MPSFRFs created by striking a structure at a particular drive point can be used to predict the behavior of the structure when it is excited at a random drive point. Even so, the resulting MPSFRFs are noisy, especially at higher frequencies. This noisiness can be due to a host of reasons, and in addition to being aesthetically displeasing, the noisiness may also create some inconsistencies in prediction. Creating an "averaged"

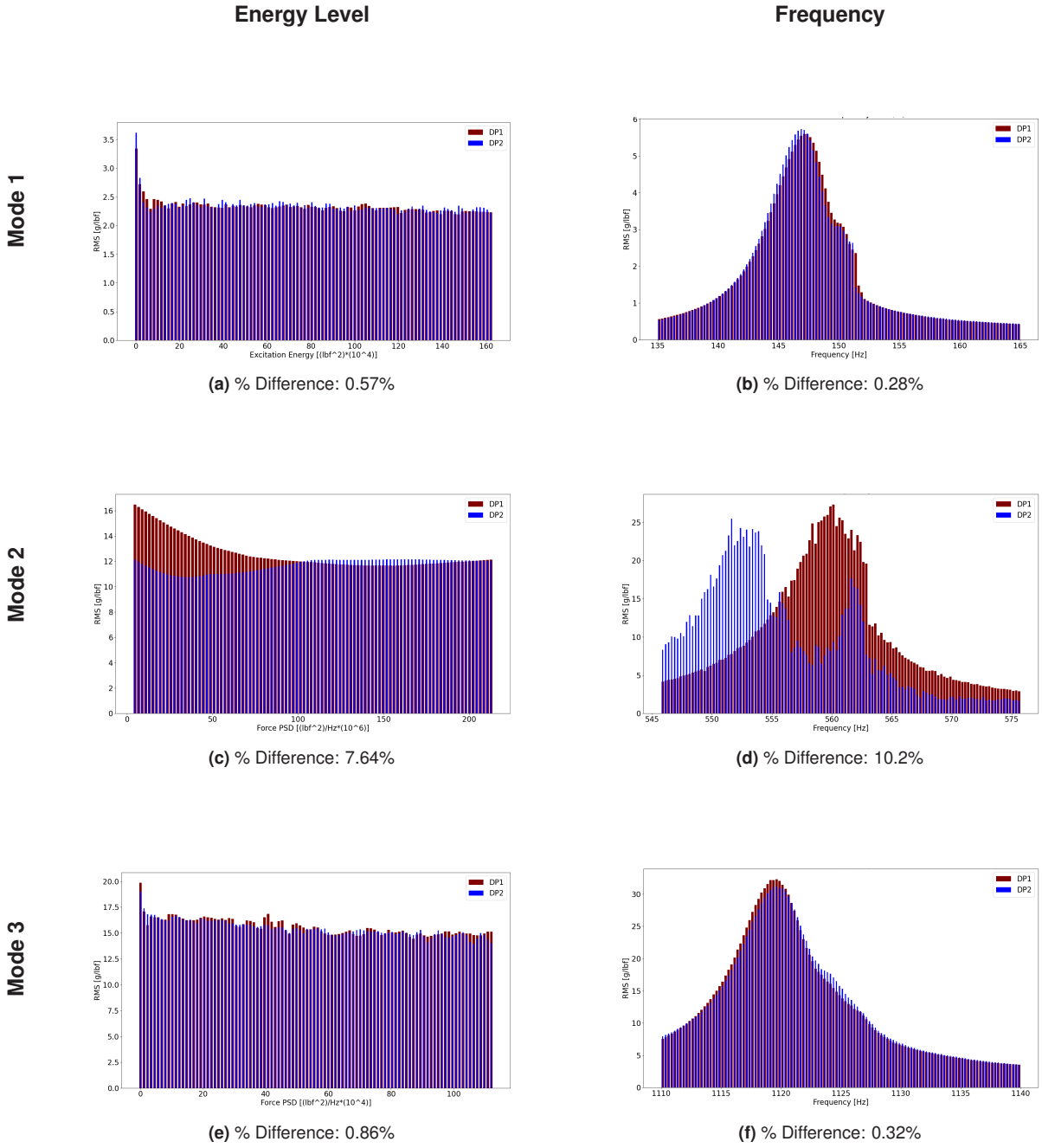

(a) % Difference: 0.57%

(b) % Difference: 0.28%

(c) % Difference: 7.64%

(d) % Difference: 10.2%

(e) % Difference: 0.86%

(f) % Difference: 0.32%

Fig. 6: RMS Error Metrics by Mode

Table 1: Error Metrics for the MPSFRFs

	Mode 1	Mode 2	Mode 3
RMS % Difference (Excitation Energy)	0.57%	7.46%	0.86%
RMS % Difference (Frequency Line)	0.23%	10.2%	0.32%
CSAC	0.97	0.88	0.99

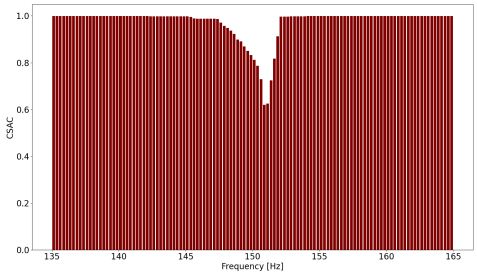

(a) Mode 1 – Mean CSAC: 0.97

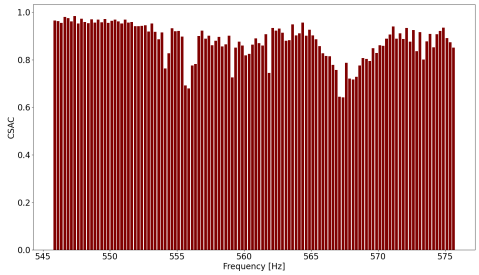

(b) Mode 2 – Mean CSAC: 0.88

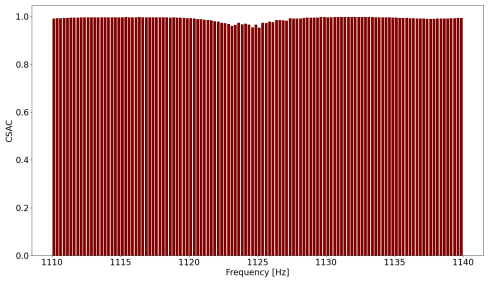

(c) Mode 3 – Mean CSAC: 0.99

Fig. 7: CSAC Error Metrics by Mode

MPSFRF can both improve the visual quality of the surface and provide a method for more consistent behavioral predictions.

To create an averaged MPSFRF, a set number of datasets are placed in different "bins" that are used to create a representative FRF. For example, suppose a bin-size of five is selected. After sorting, the first five datasets are placed in a bin, the next five datasets are placed in a separate bin, and so on until all datasets are exhausted. The combined reference and response data of each bin is used to create an FRF that is representative of the bin behavior. In this way, most of the local differences in the individual FRFs are averaged out. As a result, the representative FRFs produce a MPSFRF that is less noisy. For this experiment, bin sizes of both five and ten were used to create an averaged MPSFRF for the drive point 1 data. The average MPSFRFs are shown in Fig. 8. Clearly, the averaged MPSFRFs are smoother than the unaveraged MPSFRF displayed in Fig. 5.

The same error metrics used in Section 4.1 can be used to compare the averaged MPSFRF to its unaveraged counterpart at the same drive point. These metrics are recorded in Table 2. From the table, all the RMS percent differences for each mode are lower than two percent. For the case of mode 1 and mode 2, these percent differences are less than or equal to one percent. Furthermore, the CSAC values are greater than 0.9 in all cases. These metrics signify good agreement between the averaged and unaveraged MPSFRFs in terms of total energy content and shape. Finally, notice the averaged MPSFRF created using a bin size of five captures information about the total energy more accurately but seems to retain shape information less accurately. The decrease in RMS percent difference is expected since smaller bin sizes average less content than larger bin sizes. However, the decrease in CSAC values is puzzling. This could be because using a smaller bin size amplifies "local" noise more than using a larger bin size. Hence, the noisiness of the unaveraged and "lightly" averaged MPSFRF may result in larger differences in shape than those that exist between an unaveraged and less noisy "heavily" averaged MPSFRF.

4.3 Log-Scale Excitation Energy

Although the MPSFRFs provide an informative visual representation of the linear-to-nonlinear transition in the test object's behavior, the transition is quickly followed by a relatively stable trend in nonlinear behavior. This makes the nonlinear transitory behavior difficult to discern visually. To better depict the transition to nonlinear behavior, the MPSFRFs for drive point 1 are plotted with the excitation energy axis in log-scale. Since this exacerbated the apparent noisiness of the MPSFRFs, the plots are averaged using bin sizes of five. The resulting plots in Fig. 9 reveal this simple change makes the nonlinear behavior easier to visually observe.

The ability to create MPSFRFs with both linear- and log-scale excitation energy axes begs the question as to which method results in surfaces with greater similarity. To answer this question, error metric data is collected for

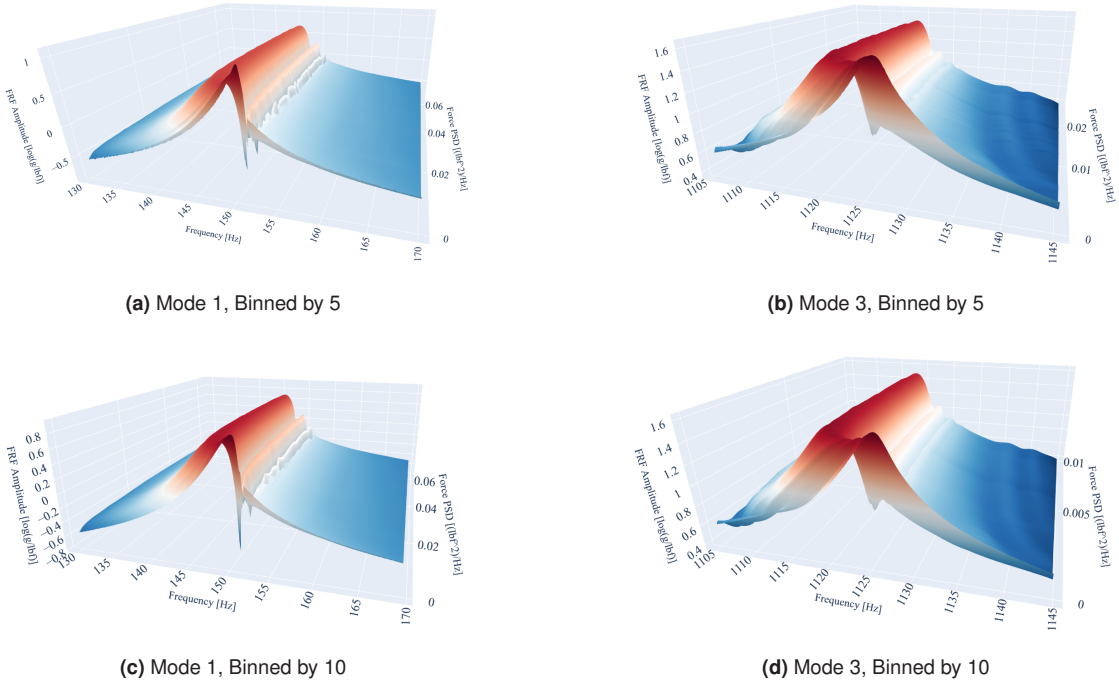

(a) Mode 1, Binned by 5

(b) Mode 3, Binned by 5

(c) Mode 1, Binned by 10

(d) Mode 3, Binned by 10

Fig. 8: Averaged MPSFRFs

Table 2: Error Metrics for Averaged vs. Unaveraged MPSFRFs for Drive Point 1

		Mode 1	Mode 2	Mode 3
Binned by 10	**RMS % Difference (Excitation Energy)**	0.67%	0.63%	0.42%
	RMS % Difference (Frequency Line)	1.00%	1.32%	0.81%
	CSAC	0.96	0.95	0.95
Binned by 5	**RMS % Difference (Excitation Energy)**	0.24%	0.45%	0.29%
	RMS % Difference (Frequency Line)	0.45%	1.08%	0.55%
	CSAC	0.94	0.94	0.94

MPSFRFs created using linear- and log-scale excitation energy axes. The resulting error metrics are presented in Table 3. Although the metrics are very similar, MPSFRFs created using linear excitation energy axes are more similar. This is most likely due to differences in the transitional region between the two surfaces being aggravated by plotting the excitation energy axes in log-scale. As a result, though log-scale MPSFRFs may be more aesthetically desirable in some cases, predictions should be made using linear-scale MPSFRFs.

5 Conclusions

The creation of three-dimensional modal performance surface FRFs (MPSFRFs) provides a novel way of visualizing and quantifying the behavior of weakly nonlinear structures. By converting the physical response data to the modal space before creating these surfaces, the PSFRFs become drive point agnostic. As a result, MPSFRFs can be used to predict the nonlinear behavior of structures impacted at random locations by transforming physical input forces into modal forces and analyzing the nonlinear response on a mode-by-mode basis, provided the impact location is sufficiently removed from the node points of the structure. By averaging small groups of individual FRFs to create an averaged MPSFRF, the noise affecting the MPSFRF can be reduced, resulting in smoother MPSFRFs that provide

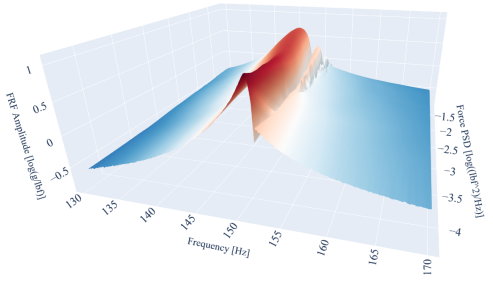

(a) Mode 1

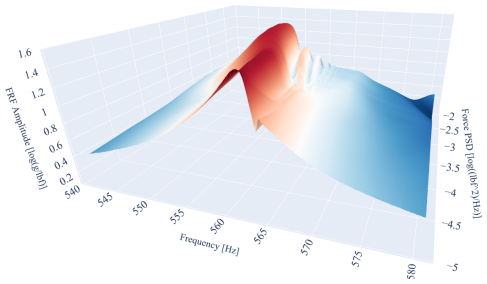

(b) Mode 2

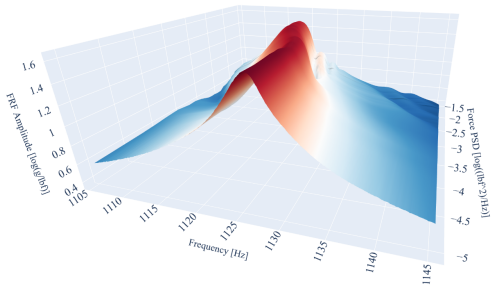

(c) Mode 3

Fig. 9: Log-Scale MPSFRFs

more consistent estimates of nonlinear behavior.

6 Future Work

The work completed in this paper only includes excitation caused by modal hammers for weakly nonlinear systems. This method should work well when the modal filter performs proper filtering, which occurs when the modes remain uncoupled and the mode shapes do not change significantly. More work needs to be done to determine how effective this method is at assessing strongly nonlinear systems. Perhaps a method similar to that developed in [60] could be iterated to determine the frequency bounds of the APSD area calculations which optimize the step of sorting individual FRFs for the construction of an MPSFRF.

To assess the feasibility of using MPSFRFs to predict sustained vibrational excitation, modal shakers will be used to excite the test object. The resulting MPSFRFs created with data obtained by a modal shaker will be used to determine how they differ from those created with modal hammer data and provide clues as to how the two classes of MPSFRFs can inform each other. Di Maio's work will prove useful in helping develop a methodology for the comparison [55].

During the analysis, it was discovered that MPSFRFs obtained from data contained sufficiently near a node point can result in scaling errors that lead to large discrepancies between two MPSFRFs associated with the same mode. More testing must be conducted to determine the distance of an excitation from a node point which is necessary for the results to remain valid. Furthermore, such experimentation will provide more insight into the scaling of MPSFRFs in general. As this work is being conducted, more error metrics may be tested to validate the similarly of corresponding MPSFRFs and determine which error metrics are superior.

Recall that the CSAC was presented in Marinone and Moya [57] and is used to represent the similarity in shape between two different FRFs (and an average CSAC value is used to validate the similarity in shape of two MPSFRFs). The CSAC evaluation metric is centered around the shifting nonlinear resonance, but harmonics could distort this evaluation with increasing distance from resonance in the frequency space. Future work should develop a metric that accounts for the full frequency spectrum, including the harmonics.

Finally, more work must be done to assess the effects of time-variability on MPSFRF creation. The boundary conditions and internal equilibria of an experimental assembly can change from day-to-day, or even hour-to-hour, depending on the input excitation and the testing environment. Since data collection can be a long process, more research needs to be conducted to determine the viability of MPSFRF creation when data is collected over an

Table 3: Error Metrics Between Drive Points 1 and 2 (Linear- and Log-Scale)

		Mode 1	Mode 2	Mode 3
Linear-Scale	RMS % Difference (Excitation Energy)	1.27%	3.56%	0.31%
	RMS % Difference (Frequency Line)	0.94%	5.81%	0.99%
	CSAC	0.97	0.85	0.99
Log-Scale	RMS % Difference (Excitation Energy)	2.07%	3.33%	2.42%
	RMS % Difference (Frequency Line)	1.18%	10.7%	1.06%
	CSAC	0.98	0.87	0.99

extended period of time.

Authors' Contributions

Caleb Bengs set up and conducted the experiment, analyzed the data, and wrote the manuscript. Daniel Roettgen designed and oversaw the experiment, and provided technical guidance. Benjamin Moldenhauer provided technical guidance in the areas of modal filtering and data sampling. All authors reviewed the final manuscript.

Acknowledgements

Sandia National Laboratories is a multi-mission laboratory managed and operated by National Technology & Engineering Solutions of Sandia, LLC (NTESS), a wholly owned subsidiary of Honeywell International Inc., for the U.S. Department of Energy's National Nuclear Security Administration (DOE/NNSA) under contract DE-NA0003525. This written work is authored by an employee of NTESS. The employee, not NTESS, owns the right, title and interest in and to the written work and is responsible for its contents. Any subjective views or opinions that might be expressed in the written work do not necessarily represent the views of the U.S. Government. The publisher acknowledges that the U.S. Government retains a non-exclusive, paid-up, irrevocable, world-wide license to publish or reproduce the published form of this written work or allow others to do so, for U.S. Government purposes. The DOE will provide public access to results of federally sponsored research in accordance with the DOE Public Access Plan.

References

[1] T. Karaağaçlı and H. N. Özgüven. Experimental modal analysis of nonlinear systems by using response-controlled stepped-sine testing. *Mechanical Systems and Signal Processing*, 146:107023, 2021.

[2] E. Petrov and D. Ewins. Analytical formulation of friction interface elements for analysis of nonlinear multi-harmonic vibrations of bladed disks. *J. Turbomach.*, 125(2):364–371, 2003.

[3] W. Szemplińska-Stupnicka. The modified single mode method in the investigations of the resonant vibrations of non-linear systems. *Journal of Sound and Vibration*, 63(4):475–489, 1979.

[4] M. Krack, L. Panning-von Scheidt, and J. Wallaschek. A method for nonlinear modal analysis and synthesis: Application to harmonically forced and self-excited mechanical systems. *Journal of Sound and Vibration*, 332(25):6798–6814, 2013.

[5] S. W. Shaw and C. Pierre. Normal modes for non-linear vibratory systems. *Journal of sound and vibration*, 164(1):85–124, 1993.

[6] D. Jiang, C. Pierre, and S. Shaw. Nonlinear normal modes for vibratory systems under harmonic excitation. *Journal of sound and vibration*, 288(4-5):791–812, 2005.

[7] C. Touzé and M. Amabili. Nonlinear normal modes for damped geometrically nonlinear systems: Application to reduced-order modelling of harmonically forced structures. *Journal of sound and vibration*, 298(4-5):958–981, 2006.

[8] E. Pesheck, C. Pierre, and S. W. Shaw. A new Galerkin-based approach for accurate non-linear normal modes through invariant manifolds. *Journal of sound and vibration*, 249(5):971–993, 2002.

[9] G. Kerschen, J.-c. Golinval, A. F. Vakakis, and L. A. Bergman. The method of proper orthogonal decomposition for dynamical characterization and order reduction of mechanical systems: an overview. *Nonlinear dynamics*, 41:147–169, 2005.

[10] R. J. Kuether and M. S. Allen. Computing nonlinear normal modes using numerical continuation and force appropriation. In *International Design Engineering Technical Conferences and Computers and Information in Engineering Conference*, volume 45004, pages 329–340. American Society of Mechanical Engineers, 2012.

[11] G. Kerschen, M. Peeters, J.-C. Golinval, and A. F. Vakakis. Nonlinear normal modes, Part I: A useful framework for the structural dynamicist. *Mechanical systems and signal processing*, 23(1):170–194, 2009.

[12] M. Peeters, R. Viguié, G. Sérandour, G. Kerschen, and J.-C. Golinval. Nonlinear normal modes, Part II: Toward a practical computation using numerical continuation techniques. *Mechanical systems and signal processing*, 23(1):195–216, 2009.

[13] D. Laxalde and F. Thouverez. Complex non-linear modal analysis for mechanical systems: application to turbomachinery bladings with friction interfaces. *Journal of sound and vibration*, 322(4-5):1009–1025, 2009.

[14] M. Feldman. Non-linear system vibration analysis using Hilbert transform–I. Free vibration analysis method'Freevib'. *Mechanical systems and signal processing*, 8(2):119–127, 1994.

[15] D. J. Segalman. A modal approach to modeling spatially distributed vibration energy dissipation. Technical report, Sandia National Laboratories (SNL), Albuquerque, NM, and Livermore, CA . . . , 2010.

[16] B. J. Deaner. *Modeling the nonlinear damping of jointed structures using modal models*. PhD thesis, University of Wisconsin–Madison, 2013.

[17] R. L. Mayes, B. R. Pacini, and D. R. Roettgen. A modal model to simulate typical structural dynamic nonlinearity. In *Dynamics of Coupled Structures, Volume 4: Proceedings of the 34th IMAC, A Conference and Exposition on Structural Dynamics 2016*, pages 57–76. Springer, 2016.

[18] W. D. Iwan. A distributed-element model for hysteresis and its steady-state dynamic response, 1966.

[19] D. J. Segalman and M. J. Starr. Iwan models and their provenance. In *International Design Engineering Technical Conferences and Computers and Information in Engineering Conference*, volume 45004, pages 441–449. American Society of Mechanical Engineers, 2012.

[20] D. J. Segalman. A four-parameter Iwan model for lap-type joints, 2005.

[21] B. J. Deaner, M. S. Allen, M. J. Starr, and D. J. Segalman. Investigation of modal Iwan models for structures with bolted joints. In *Topics in Experimental Dynamic Substructuring, Volume 2: Proceedings of the 31st IMAC, A Conference on Structural Dynamics, 2013*, pages 9–25. Springer, 2013.

[22] J. Lee. Estimation Modal Parameter Variation with Respect to Internal Energy Variation Based on the Iwan Model. *Applied Sciences*, 9(20):4290, 2019.

[23] M. Rajaei and H. Ahmadian. Development of generalized Iwan model to simulate frictional contacts with variable normal loads. *Applied Mathematical Modelling*, 38(15-16):4006–4018, 2014.

[24] M. Brake. A reduced Iwan model that includes pinning for bolted joint mechanics. *Nonlinear Dynamics*, 87:1335–1349, 2017.

[25] S. Smith, J. C. Bilbao-Ludena, S. Catalfamo, M. Brake, P. Reuß, et al. The effects of boundary conditions, measurement techniques, and excitation type on measurements of the properties of mechanical joints. In *Nonlinear Dynamics, Volume 1: Proceedings of the 33rd IMAC, A Conference and Exposition on Structural Dynamics, 2015*, pages 415–431. Springer, 2016.

[26] T. Dossogne, T. Jerome, D. Lancereau, S. A. Smith, M. Brake, et al. Experimental assessment of the influence of interface geometries on structural dynamic response. In *Dynamics of Coupled Structures, Volume 4: Proceedings of the 35th IMAC, A Conference and Exposition on Structural Dynamics 2017*, pages 255–261. Springer, 2017.

[27] M. R. Brake and P. Reuß. The Brake-Reuß beams: a system designed for the measurements and modeling of variability and repeatability of jointed structures with frictional interfaces. *The Mechanics of Jointed Structures: Recent Research and Open Challenges for Developing Predictive Models for Structural Dynamics*, pages 99–107, 2018.

[28] G. Kerschen, K. Worden, A. F. Vakakis, and J.-C. Golinval. Past, present and future of nonlinear system identification in structural dynamics. *Mechanical systems and signal processing*, 20(3):505–592, 2006.

[29] J.-P. Noël and G. Kerschen. Nonlinear system identification in structural dynamics: 10 more years of progress. *Mechanical Systems and Signal Processing*, 83:2–35, 2017.

[30] P. Saad, A. Al Majid, F. Thouverez, and R. Dufour. Equivalent rheological and restoring force models for predicting the harmonic response of elastomer specimens. *Journal of sound and vibration*, 290(3-5):619–639, 2006.

[31] J.-P. Noël, L. Renson, and G. Kerschen. Complex dynamics of a nonlinear aerospace structure: experimental identification and modal interactions. *Journal of Sound and Vibration*, 333(12):2588–2607, 2014.

[32] D. A. Ehrhardt and M. S. Allen. Measurement of nonlinear normal modes using multi-harmonic stepped force appropriation and free decay. *Mechanical Systems and Signal Processing*, 76:612–633, 2016.

[33] J. Wright, J. Cooper, and M. Desforges. Normal-mode force appropriation—theory and application. *Mechanical Systems and Signal Processing*, 13(2):217–240, 1999.

[34] O. C. Zienkiewicz, R. L. Taylor, and J. Z. Zhu. *The finite element method: its basis and fundamentals*. Elsevier, 2005.

[35] M. Narayanan, S. Narayanan, and C. Padmanabhan. Multiharmonic excitation for nonlinear system identification. *Journal of sound and vibration*, 311(3-5):707–728, 2008.

[36] I. J. Leontaritis and S. A. Billings. Input-output parametric models for non-linear systems part I: deterministic non-linear systems. *International journal of control*, 41(2):303–328, 1985.

[37] I. Leontaritis and S. A. Billings. Input-output parametric models for non-linear systems part II: stochastic non-linear systems. *International journal of control*, 41(2):329–344, 1985.

[38] S. da Silva, S. Cogan, and E. Foltête. Nonlinear identification in structural dynamics based on Wiener series and Kautz filters. *Mechanical Systems and Signal Processing*, 24(1):52–58, 2010.

[39] A. Chatterjee and N. S. Vyas. Non-linear parameter estimation in multi-degree-of-freedom systems using multi-input Volterra series. *Mechanical Systems and Signal Processing*, 18(3):457–489, 2004.

[40] R. S. Bayma, Y. Zhu, and Z.-Q. Lang. The analysis of nonlinear systems in the frequency domain using nonlinear output frequency response functions. *Automatica*, 94:452–457, 2018.

[41] H. Liang, H. Lu, K. Feng, Y. Liu, J. Li, et al. Application of the improved NOFRFs weighted contribution rate based on KL divergence to rotor rub-impact. *Nonlinear Dynamics*, 104:3937–3954, 2021.

[42] Z. Lang* and S. Billings. Energy transfer properties of non-linear systems in the frequency domain. *International Journal of Control*, 78(5):345–362, 2005.

[43] R. M. Rosenberg. Normal modes of nonlinear dual-mode systems. *Journal of Applied Mechanics*, 27(2):263–268, 06 1960. ISSN 0021-8936. doi:10.1115/1.3643948.

[44] R. M. Rosenberg. The normal modes of nonlinear n-degree-of-freedom systems. *Journal of Applied Mechanics*, 29(1):7–14, 03 1962. ISSN 0021-8936. doi:10.1115/1.3636501.

[45] R. Rosenberg. On nonlinear vibrations of systems with many degrees of freedom. *Advances in applied mechanics*, 9: 155–242, 1966.

[46] A. F. Vakakis, L. I. Manevitch, Y. V. Mikhlin, V. N. Pilipchuk, and A. A. Zevin. *Normal modes and localization in nonlinear systems*. Wiley, New York, 1996.

[47] A. Vakakis. Non-linear normal modes (nnms) and their applications in vibration theory: an overview. *Mechanical systems and signal processing*, 11(1):3–22, 1997.

[48] A. F. Vakakis, O. V. Gendelman, L. A. Bergman, D. M. McFarland, G. Kerschen, et al. *Nonlinear targeted energy transfer in mechanical and structural systems*, volume 156. Springer Science & Business Media, 2008.

[49] G. Kerschen, Y. S. Lee, A. F. Vakakis, D. M. McFarland, and L. A. Bergman. Irreversible passive energy transfer in coupled oscillators with essential nonlinearity. *SIAM Journal on Applied Mathematics*, 66(2):648–679, 2005.

[50] N. E. Huang, Z. Shen, S. R. Long, M. C. Wu, H. H. Shih, et al. The empirical mode decomposition and the hilbert spectrum for nonlinear and non-stationary time series analysis. *Proceedings of the Royal Society of London. Series A: mathematical, physical and engineering sciences*, 454(1971):903–995, 1998.

[51] M. Kurt, M. Eriten, D. M. McFarland, L. A. Bergman, and A. F. Vakakis. Strongly nonlinear beats in the dynamics of an elastic system with a strong local stiffness nonlinearity: Analysis and identification. *Journal of Sound and Vibration*, 333(7):2054–2072, 2014.

[52] K. J. Moore, M. Kurt, M. Eriten, D. M. McFarland, L. A. Bergman, et al. Time-series-based nonlinear system identification of strongly nonlinear attachments. *Journal of Sound and Vibration*, 438:13–32, 2019.

[53] M. S. Allen and R. L. Mayes. Estimating the degree of nonlinearity in transient responses with zeroed early-time fast fourier transforms. *Mechanical Systems and Signal Processing*, 24(7):2049–2064, 2010.

[54] J. B. Allen and L. R. Rabiner. A unified approach to short-time fourier analysis and synthesis. *Proceedings of the IEEE*, 65 (11):1558–1564, 2005.

[55] D. Di Maio. A novel analysis method for calculating nonlinear Frequency Response Functions. *Journal of Structural Dynamics*, (3):30–57, 2025.

[56] S. Spottswood and R. Allemang. On the investigation of some parameter identification and experimental modal filtering issues for nonlinear reduced order models. *Experimental mechanics*, 47(4):511–521, 2007.

[57] T. Marinone and A. Moya. Comparison of FRF correlation techniques. In *Model Validation and Uncertainty Quantification, Volume 3: Proceedings of the 33rd IMAC, A Conference and Exposition on Structural Dynamics, 2015*, pages 299–309. Springer, 2015.

[58] D. P. Rohe and R. Schultz. A Custom Multi-Axis Vibration Controller with Flexible Control Strategies. Technical report, Sandia National Lab.(SNL-NM), Albuquerque, NM (United States), 2020.

[59] K. Coletti, R. Schultz, and S. Carter. A practitioner's guide to local frf estimation. In D. Di Maio, editor, *Special Topics in Structural Dynamics & Experimental Techniques, Vol. 5*, pages 67–80, Cham, 2024. Springer Nature Switzerland. ISBN 978-3-031-68901-7.

[60] K. J. Moore, M. Kurt, M. Eriten, D. M. McFarland, L. A. Bergman, et al. Wavelet-bounded empirical mode decomposition for measured time series analysis. *Mechanical Systems and Signal Processing*, 99:14–29, 2018.